

Investigating the Andromeda Stream: II. Orbital Fits and Properties of the Progenitor

M. A. Fardal^{1,2*}, A. Babul¹, J. J. Geehan¹, and P. Guhathakurta³

¹*Dept. of Physics & Astronomy, University of Victoria, Elliott Building, 3800 Finnerty Rd., Victoria, BC, V8P 1A1, Canada*

²*Dept. of Astronomy, University of Massachusetts, Amherst, MA, 01003, USA*

³*UCO/Lick Observatory, Dept. of Astronomy & Astrophysics, Univ. of California, 1156 High St., Santa Cruz, CA, 95064, USA*

Accepted 2005 November 10. Received 2005 October 30; in original form 2005 January 13

ABSTRACT

We construct test-particle orbits and simple N-body models that match the properties of the giant stellar stream observed to the south of M31, using the model of M31’s potential derived in the companion paper by Geehan et al. (2005). We introduce a simple approximation to account for the difference in position between the stream and the orbit of the progenitor; this significantly affects the best-fitting orbits. The progenitor orbits we derive have orbital apocenter ~ 60 kpc and pericenter ~ 3 kpc, though these quantities vary somewhat with the current orbital phase of the progenitor which is as yet unknown. Our best combined fit to the stream and galaxy properties implies a mass within 125 kpc of M31 of $(7.4 \pm 1.2) \times 10^{11} M_{\odot}$. Based on its length, width, luminosity, and velocity dispersion, we conclude that the stream originates from a progenitor satellite with mass $M_s \sim 10^9 M_{\odot}$, and at most modest amounts of dark matter; the estimate of M_s is again correlated with the phase of the progenitor. M31 displays a large number of faint features in its inner halo which may be progenitors or continuations of the stream. While the orbital fits are not constrained enough for us to conclusively identify the progenitor, we can identify several plausible candidates, of which a feature in the planetary nebula distribution found by Merrett et al. is the most plausible, and rule out several others. We make predictions for the kinematic properties of the successful candidates. These may aid in observational identification of the progenitor object, which would greatly constrain the allowed models of the stream.

Key words: galaxies: individual: M31 – galaxies: interactions – galaxies: kinematics and dynamics

1 INTRODUCTION

The giant southern stream observed near the Andromeda galaxy (M31) provides us with an extraordinary opportunity to study the disruption by a large disk galaxy of one of its satellite galaxies, and thereby obtain a sensitive probe of the dynamics in M31. The stream was originally discovered through counts of red giant stars in the M31 halo (Ibata et al. 2001a). Later extensions of this survey (Ferguson et al. 2002; McConnachie et al. 2003; Ferguson et al. 2004) outlined the extent of the stream from a projected distance of 60 kpc from the center of M31 on the southern side, to a possible extension on the northern side of M31. Fits to the tip of the red giant branch (McConnachie et al. 2003) provided line-of-sight distances as a function of position along the stream. Finally, spectroscopy of stars along the path of the stream (Ibata et al. 2004; Guhathakurta et al. 2005) has resolved the stream as a distinct kinematic component as well, and has also provided absorption-line estimates of the metallicity of the stream stars. The stream resembles

the extended tidal tails of the Sagittarius dwarf galaxy that wrap around the Milky Way (Totten & Irwin 1998), though its azimuthal extent around M31 is much smaller. A major difference is that we do not know if the progenitor of the Andromeda stream has survived and if so where it is, although several faint features in the inner halo of M31 have been suggested as possible progenitors.

Since the three-dimensional path of the stream is now measured along with one velocity component, we have nearly complete information on the path of the system in phase space. If we combine the stream data with other observations of M31 such as its rotation curve, we should be able to obtain a direct estimate of the gravitational potential in the M31 halo, as well as follow the path of the stream beyond the visible southern portion. Current work includes some first steps in this direction. Font et al. (2005) computed orbits in a bulge-disk-halo model. These authors found rough consistency of their potential with the stream, but they did not optimize the agreement in detail, focusing instead on the physical implications of the width and velocity dispersion of the stream. Ibata et al. (2004) tested several potentials, deriving a weakly model-dependent limit on the mass within 125 kpc. They supplied model parameters only for their simple spherical po-

* E-mail: fardal@fcrao1.astro.umass.edu, babul@uvic.ca, jgee-han@uvic.ca, raja@ucolick.org

tentials, which have the disadvantage that they do not match the M31 rotation curve. They used a more sophisticated bulge-disk-halo model as well, but this is not fully specified in the paper.

An issue that deserves closer attention is the slight difference between the locations of the orbit and the stream. Both Ibata et al. (2004) and Font et al. (2005) assume for simplicity that the stream follows the orbit. However, the stream exists precisely because its constituent stars are on slightly *different* orbits. The systematic variation of orbital energy along the stream, which is accounted for implicitly by N-body simulations but not by simple orbital integrations, may affect the estimates of the M31 potential and the trajectory of the progenitor. Hence it is worth building upon the earlier work to construct a more specific and more accurate model of the stream.

In Geehan et al. (2005) (Paper I), we presented a simple analytic bulge-disk-halo model for the potential of M31, fitted to observed tracers of the potential ranging from bulge stars to satellites in the outer halo, and we quantified the error on the model parameters. In this paper, we use this fit to derive simple models of the southern stream, and discuss their physical implications. We start off with a subset of the observational data and then gradually add in more constraints. In § 2, we consider the orbital information alone. We integrate orbits in our M31 potential to obtain best values and confidence intervals for the orbital parameters, and further refine the galactic parameters compared to Paper I. We introduce an approximate method to calculate the phase space location of the stream given the orbit of the progenitor, test it with N-body simulations, and incorporate it within the fitting procedure; as a result the allowed orbits are changed considerably. In § 3, we add in the constraints that the observed length, width, velocity dispersion, and luminosity of the stream put on the properties and current location of the progenitor satellite, using N-body simulations that follow our best-fitting orbit. § 4 examines the forward continuation of the stream, including the progenitor location, and its relation to the orbital characteristics of the stream. Among the numerous faint features in the inner halo of M31, we can identify some that are plausibly related to the stream. Finally, § 5 presents our conclusions.

2 ORBITAL FITS

2.1 Summary of the observations

Though it was discovered only recently, the variety of observational information about the southern stream already approaches that which is available for the Sagittarius stream in our own galaxy. We review here what is currently known about the configuration of M31 and the southern stream.

We look at the M31 galaxy from below, as is evident from images of the disk’s dust lanes projected on the bulge, and the galaxy spins counterclockwise on the sky. We take the inclination of M31 to be 77° , and the position angle to be 37° . We use a distance to M31 of $z_g = 784 \pm 24$ kpc (Stanek & Garnavich 1998), and a mean radial velocity of $v_{gz} = -300 \pm 4$ km s $^{-1}$ (de Vaucouleurs et al. 1991).

Because the M31-stream system covers such a large region on the sky, its transverse velocity is one of the primary uncertainties in its internal kinematics, which is a situation rarely encountered in astronomy. Since M31 and the Milky Way are the primary mass concentrations in the Local Group, it is traditionally assumed that they are falling in toward each other for the first time, so that the transverse velocity is much smaller than the ra-

dial velocity. We prefer to use the results of Peebles et al. (2001), who have modeled the Local Group dynamics in detail. They found solutions for M31’s transverse velocity falling mostly into two clumps in opposing directions, with velocities in supergalactic coordinates l and b of either $(v_{gl}, v_{gb}) = (-40, 120)$ km s $^{-1}$ or $(30, -140)$ km s $^{-1}$. The eastward and northward velocities are then $(v_{gx}, v_{gy}) = (-130, 20)$ km s $^{-1}$ or $(150, 0)$ km s $^{-1}$. The dominance of the east-west component stems from the direction of the local filament, along which M31 tends to move in the Peebles et al. model.

The giant southern stream extends to the SE of the galaxy for approximately 5° . The total extent of the stream is not well known; at its southern end it *may* be visibly petering out close to Field 1 of McConnachie et al. (2003), as seen in the larger survey presented in Ferguson et al. (2004), and continuing northwards it is eventually lost to confusion against the M31 disk. The stream luminosity is $\sim 3.4 \times 10^7 L_\odot$ (Ibata et al. 2001a), suggesting a stellar mass $\sim 2.4 \times 10^8 M_\odot$ if we assume $M/L_V \approx 7$. The mean metallicity of the stream is $[\text{Fe}/\text{H}] \approx -0.5$ (Guhathakurta et al. 2005), suggesting the progenitor had a much larger total luminosity of $\sim 10^9 L_\odot$ (Font et al. 2005). McConnachie et al. suggest the stream continues at least 1.5° to the NW on the near side of M31, but this is questionable for several reasons: the purported extension is not a distinct surface brightness feature (Ferguson et al. 2004), there is as yet no spectroscopic confirmation of a stream component, and as shown in Ibata et al. (2004) it is difficult to derive an orbit that fits this feature. We therefore consider this “northern extension” to be just one of many faint features that could possibly be extensions of the stream. In contrast, the reality of the southern portion is in no doubt, due to the strong enhancement in star counts and observation of a distinct kinematic component in five spectroscopic fields along the stream.

Field coordinates for the published observations of the stream are listed in Table 1, along with distances and velocities of the stream. The positions show the stream is a roughly linear structure, at least in projection. The field “a3” of Guhathakurta et al. (2005) overlaps the stream only by chance, and is not centered on the stream. McConnachie et al. (2003) chose their fields to lie approximately along the stream center. However, some of these positions were chosen by extrapolation from the inner part of the stream. In fact, their fig 3, showing a histogram of stars as a function of transverse position, suggests the central ridge of the stream is offset fairly uniformly by $\sim 0.15^\circ$ from the field centers, towards the SE. We use the slope of Fields 1–8 to define rotated sky coordinates m and n , where $m \equiv 0.504\xi - 0.864\eta$ increases along the stream (roughly toward the SE) and $n \equiv -0.864\xi - 0.504\eta$ increases across the stream (roughly toward the SW). We then shift the mean transverse position of the stream relative to the field centers by 0.15° . This shift is small compared to the width of the stream, approximately 0.5° wide full width at half-maximum (FWHM) on the sky or about 7 kpc in distance, as seen in the same figure. We assign an uncertainty of 0.15° to the stream’s angular position.

Distances to the M31 stream fields are given by McConnachie et al. (2003) and reproduced in Table 1. These show the stream lies further away than M31, and the stream follows a roughly radial trajectory. We exclude the fields on the northern side, and exclude the field nearest to M31 (Field 8) as well because of possible contamination by disk stars. McConnachie et al. estimate a total error of 20 kpc on their distances, but this is composed of ~ 12 kpc random error and ~ 16 kpc systematic error from the photometric zero-point and the stellar population uncertainties. Orbits that have a steeper or shallower gradient of distance along the stream than the observed gradient, as in

Table 2. Parameter choices for some orbits discussed in the text. The first six parameters give the initial position and velocity of the test particle (the orbit is calculated both forward and backward of this point). Δz is the fitted systematic offset between our distance calibration and that of McConnachie et al. (2003). The halo parameter f_h determines the strength of the galaxy potential. The final parameter gives the value of reduced χ^2 from our fit. Initial conditions 1e, 2e, 3e, and 4e give the same orbits as 1, 2, 3, and 4, except they begin at an earlier point on the orbit.

Orbit	$x(0)$ kpc	$y(0)$ kpc	$z(0)$ kpc	$v_x(0)$ km s ⁻¹	$v_y(0)$ km s ⁻¹	$v_z(0)$ km s ⁻¹	Δz kpc	f_h	F_p	χ^2/N_{deg}	comments
1	5.19	-20	38.0	-61.2	132.9	-214.4	-4.0	1.14	...	0.16	fit to orbit, variable halo
	± 1.12	...	± 8.8	± 9.4	± 21.9	± 6.7	± 12.8	...	± 0.35		
1e	-52.7	42.6	-28.2	126.5	-94.2	53.9	-4.0	1.14	...	0.16	same orbit, earlier start
2	5.60	-20	18.4	-67.9	145.2	-209.5	-21.42	1.14	1.00	0.51	fit to stream, var halo, $F_p = 1.0$
	± 1.02	...	± 2.7	± 4.0	± 13.7	± 7.3	± 6.4	± 0.37	...		
2e	-8.8	-19.1	-56.4	4.9	44.8	42.4	-21.42	1.14	1.00	0.51	same orbit, earlier
3	7.04	-20	23.6	-51.9	85.2	-155.1	-18.70	1.16	1.50	0.48	fit to stream, var halo, $F_p = 1.5$
	± 0.66	...	± 5.8	± 6.5	± 14.3	± 8.5	± 11.4	± 0.40	...		
3e	-5.5	-11.8	-42.1	5.9	45.7	53.2	-18.70	1.16	1.50	0.48	same orbit, earlier
4	5.15	-15	16.7	-59.4	102.3	-175.0	-19.88	1.10	2.00	0.46	fit to stream, var halo, $F_p = 2.0$
	± 0.51	...	± 2.8	± 4.1	± 12.0	± 7.8	± 8.0	± 0.38	± 0.00		
4e	-2.2	-7.5	-32.2	4.4	52.8	81.1	-19.88	1.10	2.00	0.46	same orbit, earlier
5	8.54	-20	29.4	-7.2	6.4	-57.7	-15.55	1.02	2.02	0.97	fit to M32
	± 0.60	...	± 2.4	± 17.9	± 28.1	± 54.5	± 5.1	± 0.32	± 0.01		
6	5.78	-20	25.7	-62.4	118.9	-196.7	-12.86	1.47	1.12	0.57	fit to Northern Spur
	± 0.93	...	± 3.3	± 7.4	± 16.8	± 9.3	± 8.1	± 0.46	± 0.03		
7	6.96	-20	25.1	-51.0	83.2	-154.5	-16.20	1.18	1.50	0.47	fit to And NE
	± 0.71	...	± 2.8	± 9.4	± 17.9	± 12.7	± 6.4	± 0.40	± 0.13		
8	5.25	-15	24.2	-63.6	136.4	-220.9	-7.07	2.21	1.29	1.00	fit to Merrett NE PNe
	± 0.52	...	± 3.2	± 8.0	± 19.2	± 7.7	± 9.1	± 0.68	± 0.04		

Table 1. Kinematic data for the southern stream, in units where M31 is at the center. A dash indicates that there is no data for that field. The angular positions ξ and η are those of the field centers; field “a3” is certainly offset from the position of the stream, while fields 1–8 may be as well.

Field	ξ (deg)	η (deg)	d' (kpc)	v'_r (km s ⁻¹)
a3	+1.077	-2.021	66	-158
1	+2.015	-3.965	102	0
2	+1.745	-3.525	93	-50
3	+1.483	-3.087	76	—
4	+1.226	-2.653	71	—
5	+0.969	-2.264	56	—
6	+0.717	-1.768	52	-180
7	+0.467	-1.327	45	—
8	+0.219	-0.886	-4	-300
12	-0.731	+0.891	-45	—
13	-0.963	+1.342	-26	—

fig. 4c of Ibata et al. (2004) or fig. 2a of Font et al. (2005), can thus be ruled out even if they lie within the total error bars of McConnachie et al. To treat this in our orbital fitting, we take the observed distances to be the McConnachie values plus a free parameter, Δz . Assuming the uncertainty on this systematic shift is $\sigma_{\Delta z} = 16$ kpc, we then include a term $(\Delta z/\sigma_{\Delta z})^2$ in the total χ^2 . We set the *random* error on each distance point equal to 12 kpc.

The mean velocity at various points along the stream has been measured in four fields along the stream by Ibata et al. (2004), and in the single stream field “a3” of Guhathakurta et al. (2005). This reveals that the stream is falling in toward M31 from behind. We again omit the field closest to M31 (Field 8 of Ibata et al.) because of contamination concerns. Guhathakurta et al. (2005) estimate the random error on their mean velocity to be 4 km s⁻¹. Ibata et al.

(2004) do not quote errors on their mean velocities, but they are probably comparable since they estimate the velocity dispersion itself to be only 11 km s⁻¹. However, the true uncertainty includes systematic effects such as the 4 km s⁻¹ error in M31’s radial velocity, and contamination by the possibly lumpy velocity distribution of the general halo population. Because of these concerns, we (somewhat arbitrarily) raise the estimate of the velocity error to 8 km s⁻¹.

Our orbits are computed in a rectangular right-handed coordinate system (x, y, z) , centered on M31 and oriented with respect to the sky so that x points east, y points north, and z points away from us. However, the observed quantities are not obtained in a rectangular coordinate system, because M31 is so close that the system has a significant width and depth on the sky. Insufficient information is available to correct all the observations to rectangular coordinates, so we convert the orbits to observed coordinates instead. The positional coordinates ξ and η are standard coordinates on the tangent plane. We obtain the east-west coordinate ξ , the north-south coordinate η , the distance d , and the radial velocity v_r using the following formulae:

$$\xi = x/(z_g + z) \quad (1)$$

$$\eta = y/(z_g + z) \quad (2)$$

$$d \equiv d' + z_g = [x^2 + y^2 + (z_g + z)^2]^{1/2} \quad (3)$$

$$v_r = d^{-1} [x(v_x + v_{gx}) + y(v_y + v_{gy}) + (z_g + z)(v_z + v_{gz})] \quad (4)$$

$$\equiv v'_r + v_{gz}$$

In our plots we use the relative distance d' (which we call the “depth”) and the relative velocity v'_r , found by subtracting the mean distance and radial velocity of M31. These equations could also be expanded in orders of M31-centric quantities, since in practice only the first-order correction terms are significant. For the two

solutions for the transverse velocity of M31 (v_{gx}, v_{gy}) discussed above, the effect of M31's transverse velocity on v_r is quite modest, only about $\pm 5 \text{ km s}^{-1}$ for Field 1 which is the most strongly affected field. This is partly because these velocity solutions point almost perpendicular to the stream. In contrast, a maximum velocity of $\pm 300 \text{ km s}^{-1}$ along the stream, as allowed for by Ibata et al. (2004), would have added a significant uncertainty of $\sim 30 \text{ km s}^{-1}$. We set $v_{gx} = v_{gy} = 0$ from now on.

2.2 Fits to stream directly

We now try to find orbits that fit the stream observations. At first, for simplicity, we assume that the stream follows the orbit, as in the work of Ibata et al. (2004) and Font et al. (2005). In Paper I, we demonstrated that even with this assumption our orbits can still differ significantly from those in the cited papers, because of the different radial mass distribution and the flattening of the disk potential. The possible flattening of the halo component is a contentious issue even in the case of the Sagittarius stream in our own Galaxy (Ibata et al. 2001b; Martínez-Delgado et al. 2004; Johnston, Law, & Majewski 2005; Law, Johnston, & Majewski 2005), which is more suitable for detecting the effects of a non-spherical potential due to its much larger azimuthal extent. In any case the disk contributes significantly to the overall flattening in the Milky Way, and thus probably in M31 as well. In this paper we will simply assume the halo is spherical, but this is certainly an issue to examine in the future.

We ignore the effect of dynamical friction on the satellite orbit. This is partly for convenience, as the strength of dynamical friction depends on the unknown mass and size of the progenitor, and thus complicates the estimates we make of these quantities in § 3 below. More importantly, we expect the effect of dynamical friction on the energy to be fairly small ($< 10\%$ per orbit) unless the progenitor satellite mass M_s is quite large ($M_s \gg 10^9 M_\odot$). Our simulations typically have $M_s \sim 10^9 M_\odot$ at the start of the run, and the effects of tidal stripping and gravitational disk shocking further reduce this mass during the run. Dynamical friction due to the disk itself is likely important only for satellites with orbits in the plane of the disk (Taylor & Babul 2001). Furthermore, for a highly radial orbit such as that required by the southern stream, the energy loss is almost entirely due to the passage through pericenter. The energy within the stream, which is observed over less than one radial period, is thus affected very little by the neglect of dynamical friction. In § 4, we speculate on the location of the progenitor allowing for the possibility that it has passed through pericenter once again. The neglect of dynamical friction there may induce a small error, the size of which depends on how much of the mass has managed to remain as an intact object during this second passage. Accounting for this would greatly complicate the analysis, so we leave treatment of dynamical friction to future work.

We also assume a static potential, ignoring any interaction with M31's satellite galaxies or recoil and/or distortion of M31's potential. The latter assumption is justified because of the large mass of M31 ($\sim 10^{11} M_\odot$ in the bulge and disk alone), compared to the typical estimated mass of the progenitor ($\sim 10^9 M_\odot$) that we estimate below. With these assumptions, the zero-point of the orbit is arbitrary. We absorb this freedom by setting the orbit to begin in a fixed plane, usually $y(0) = -20 \text{ kpc}$.

Paper I showed that there is considerable uncertainty in the potential of M31, especially in the halo regions where the stream lies. This uncertainty is mostly due to two degeneracies between the model parameters, namely a tradeoff between the disk and halo

components and between the scale radius r_h and density parameter δ_c of the halo. Much of the formally allowed region, however, implies unlikely values for the physical parameters like the halo concentration, baryonic fraction, and disk mass-to-light ratio; thus the likely region of parameter space is much smaller. Because the detailed properties of the disk and bulge are not probed by the stream, we limit our exploration of parameter space to a one-dimensional path that varies the strength of the force at large radii. We set the disk surface density to a fixed value $\Sigma_0 = 4 \times 10^8 M_\odot \text{ kpc}^{-2}$; the bulge and disk scale lengths $r_b = 0.61 \text{ kpc}$ and $r_d = 5.4 \text{ kpc}$ are already fixed by our fit to the surface brightness. (These parameters are defined completely in Paper I.) We then find the best fit values of the bulge mass M_b and the halo density parameter δ_c as a function of the halo scale radius r_h , storing them in a lookup table along with the value of χ^2 . In other words, we are probing a vertical path through the contours in fig. 6 of Paper I. For convenience, we describe the location along this path with a ‘‘halo parameter’’ $f_h \equiv r_h/r_h^{(0)}$, where $r_h^{(0)} = 9.0 \text{ kpc}$ is the best fit scale radius for the chosen Σ_0 in our flattened disk model. To within a few percent, the best-fitting bulge mass and halo density parameter along this path are given by

$$\begin{aligned} M_b &= (2.71 + 0.435u - 0.161u^2 + 0.0229u^3) \times 10^{10} M_\odot, \\ \delta_c &= \exp(12.46 - 1.928u + 0.1434u^2), \end{aligned}$$

with $u \equiv \ln f_h$. The mass within 125 kpc, approximately the maximum radius of the stream, scales roughly as $M_{125} = 6.68 \times 10^{11} f_h^{0.57} M_\odot$. The allowed deviation of δ_c from its best-fitting value is very small once the other parameters are specified, due to the small error bars on the rotation curve, so we do not try to adjust it from its best fit value to vary the halo potential further.

This gives seven free parameters to consider: $x(0)$, $z(0)$, $v_x(0)$, $v_y(0)$, $v_z(0)$, Δz , and f_h . $x(0)$ and the ratio $v_x(0)/v_y(0)$ are fairly tightly constrained by the positional data, while $v_z(0)$ is constrained by the spectroscopic data. This leaves $z(0)$ and $v_x(0)/v_z(0)$ as the most uncertain parameters, since they involve the distance measurements.

We use a simple Runge-Kutta integration procedure to trace the orbit, since extremely high accuracy over many orbital periods is not required. We use a Levenberg-Marquardt χ^2 routine to optimize the fit to the stream.

Our best-fitting orbit (labeled orbit 1 in Table 2) is shown as the solid line in Fig. 1. We also show the same orbit calculated with a constant conversion of transverse distance to angle, using the distance to M31 of 784 kpc. When this is done, the stream moves outward significantly in ξ and η because it lies further away than M31. v_r' also changes by a small amount ($\lesssim 5 \text{ km s}^{-1}$) due to the variation in the radial vector on the sky.

Our best-fitting orbit fits the data quite well; in fact, the $\chi^2 = 2.2$ for 14 degrees of freedom is almost too good. (In part, this is because the positional data points are derived from the field centers rather than calibrated individually, and thus have effectively been smoothed.) The best-fitting parameter values and their formal errors from the covariance matrix are given in Table 2. The radial period is 1.7 Gyr, apocenter is at 119 kpc, and pericenter is at 2.2 kpc. The orbit reaches apocenter near the most distant field (Field 1); this happens because the velocity relative to M31 is close to zero, requiring turnaround there. If we include only the observational constraints from the stream, the preferred halo parameter is $f_h = 1.8 \pm 1.1$, corresponding to a mass of $M_{125} = (9.1 \pm 3.1) \times 10^{11} M_\odot$. This suggests a more massive halo than in our preferred galaxy model, which has $f_h = 1.0 \pm 0.4$, or $M_{125} = (6.7 \pm 1.3) \times 10^{11} M_\odot$. The observational constraints

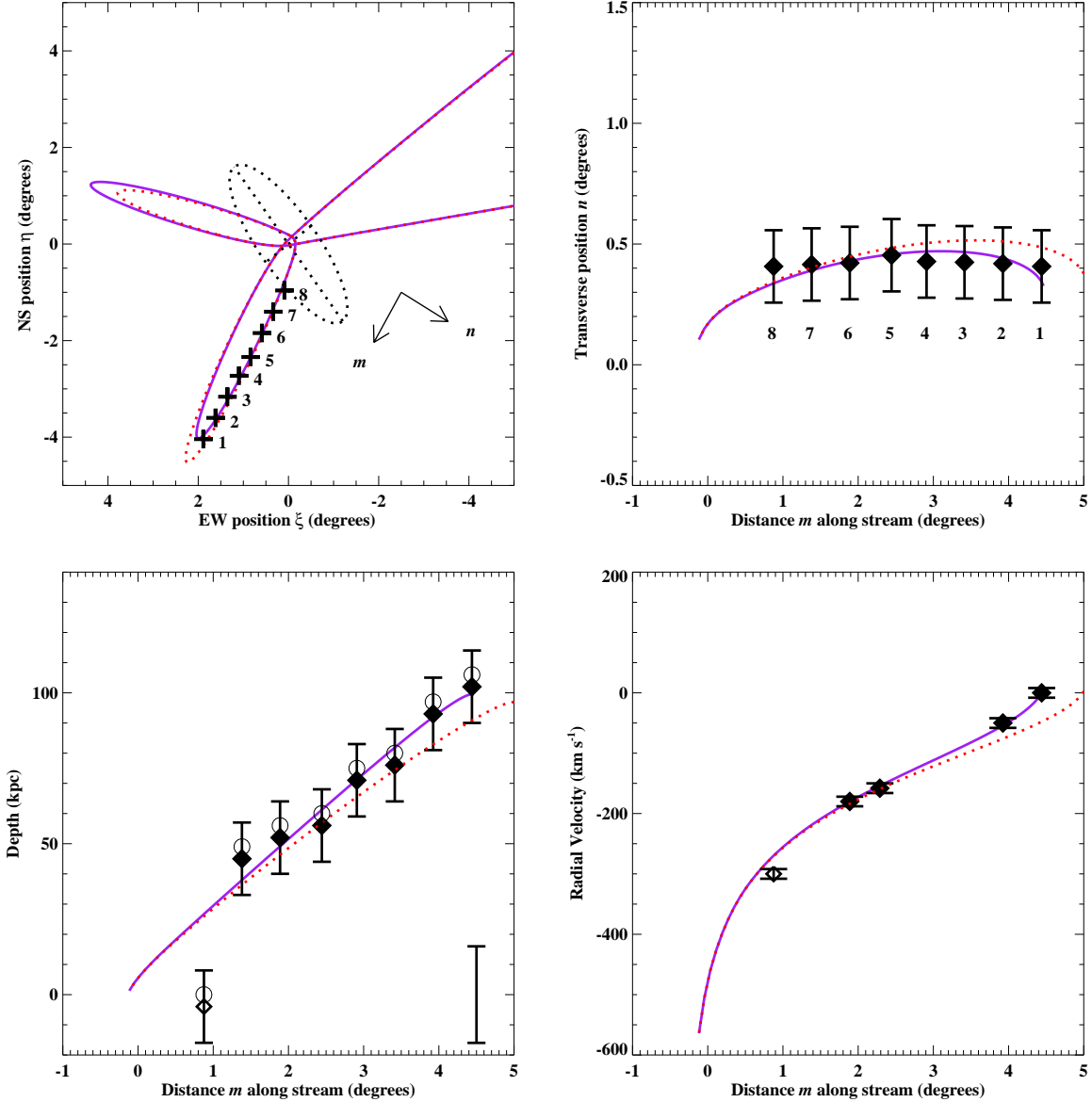


Figure 1. Best-fitting orbit assuming the stream follows the orbit, using the flattened disk potential. The orbit is shown with purple solid lines. The orbit calculated using a rectilinear coordinate system is shown with red dotted lines (see discussion in the text). Observational results are shown with black symbols. (Upper left): North-south coordinate η versus east-west coordinate ξ . The direction vectors of the stream coordinates m and n are shown in the plot. Crosses indicate the stream positions derived from the field coordinates of McConnachie et al. (2003), offset slightly as discussed in the text; the fields are labeled according to the numbering in that paper. (Upper right): Transverse stream coordinate n , versus distance along stream m , with the vertical scale expanded for clarity. Diamonds indicate the same stream positions as in the previous panel, again labeled by field number. (lower left): Depth d' relative to M31 versus m . Diamonds indicate the observational constraints of McConnachie et al. (2003), as adjusted by the systematic shift Δz from our fit; open circles give the depth values with the original calibration. The leftmost diamond is left empty as a reminder we do not use this point in the fit, due to concerns over contamination by the disk. The error bar in the bottom right corner indicates the uncertainty on Δz . (Lower right): Radial velocity v'_r , relative to M31, versus m . Diamonds indicate the observational constraints of Ibata et al. (2004) and Guhathakurta et al. (2005). The leftmost symbol is again left empty as a reminder we do not use this point in the fit.

on the galaxy fit are stronger than those on the stream, however, so when we combine the stream data with the galaxy fit the preferred halo scaling parameter is raised only slightly: $f_h = 1.1 \pm 0.3$, or $M_{125} = (7.2 \pm 1.0) \times 10^{11} M_\odot$. The fits with and without the galaxy term are both consistent with Ibata et al. (2004), who found a 1σ confidence interval of $M_{125} = (6.2\text{--}10.0) \times 10^{11} M_\odot$. The orbit is less strongly radial than in Ibata et al., which has $R_{apo} \sim 125$ kpc and $R_{peri} \sim 1.8$ kpc. It is more radial than the orbits in Font et al. (2005), which have $R_{apo} \sim 110$ kpc and $R_{peri} \sim 4$ kpc. The direction of their second loop is also signif-

icantly different. The differences between these various orbits are induced both by different assumptions about the potential of M31 and by differences in the chosen fitting technique and treatment of the observational data.

2.3 Stream-orbit tilt

The next step is to incorporate a phase space tilt between the orbit and the stream. When a satellite is tidally disrupted, stars on different orbits arrange themselves primarily as a function of

their orbital energy onto a stream that nearly follows the orbit (Johnston, Sackett, & Bullock 2001). The “nearly” is important, though: the stream is tilted relative to the progenitor’s orbit, both in 3-d real space and 6-d phase space. For an object like the Andromeda stream which is on a highly radial orbit, the stream stars are lost from the progenitor almost entirely at pericenter. If the progenitor is disrupted over the course of several radial periods, a stream results from each pericentric passage, with the youngest stream having the largest tilt relative to the orbit. (Fig. 1 in Law, Johnston, & Majewski 2005 displays these effects for a model of the Sagittarius stream.) The length of the stream increases both with time and with the scatter in the energy; this scatter depends in turn on the satellite mass. The phase space tilt between the orbit and the stream, however, decreases with time and to first order is *independent* of the satellite mass. Hence, to predict the stream location given the progenitor’s orbit, we need only to know when the stream stars were removed from the progenitor, and not the mass or other properties of the progenitor. In theory this could include pericentric passages before the last one, but this is unlikely because of the narrowness and high surface brightness of the stream (Font et al. 2005). (Note: when we refer to the “last” pericentric passage, we mean the last one experienced by the southern stream stars, unless otherwise specified. The progenitor itself may already have passed through pericenter again.)

The current location of the progenitor along the orbit thus becomes an important variable. This is currently unknown, but we can at least put some constraints on it. The progenitor is unlikely to trail the southern stream in its orbit, since there would be another stream behind it which is not observed. The progenitor is not observed along the stream, although it could be located there if it is almost entirely disrupted. However, the luminosity of the progenitor inferred from the stream’s metallicity by Font et al. (2005) is much larger than the total luminosity of the stream, suggesting this is rather unlikely. If the progenitor lies too far ahead of the stream in its orbit, on the other hand, the corresponding stream length and hence the implied scatter in the orbital energies may require a improbably large progenitor mass, as discussed below.

Suggested progenitors for the stream include the And VIII concentration, the Northern Spur, and a high-metallicity feature on the east side of the disk. All lie near the M31 disk, and thus would have to precede the stream in its orbit. If one of these was the source of the stream, one might expect that if it had passed the next pericenter and was heading inbound again, there would be an obvious continuation of the stream pointing outwards. The lack of such a feature is a weak argument that the orbital phase of the progenitor is < 1.5 . It is also possible that the progenitor lies somewhat ahead of the southern stream in the vicinity of pericenter, but is projected against M31 and has escaped detection completely. These arguments suggest the stream stars were most likely unbound from the satellite in the range 0.8–1.5 radial periods ago, at the last pericenter passage.

To fit the orbit, many orbital integrations are required, so computing the tilt between the stream and the orbit using an N-body simulation on each integration would be extremely cumbersome. We need a simple method to infer the position and velocity of the stream, given the orbit of its progenitor. Our model builds on the ideas presented in Johnston (1998). That paper shows the azimuthal phase at apocenter does not vary strongly with orbital energy, i.e., along the stream. From this observation, it infers that the azimuthal phases of the different stream orbits are self-similar. That is, the azimuthal phase Ψ of a given orbit in the stream as a function of time t past pericenter is simply $\Psi(t) = \Psi_0 + \Psi_{cen}(t/\tau + t_0)$, where Ψ_{cen} is the phase of the central orbit, the time scaling factor τ

depends on the orbital energy, and t_0 and Ψ_0 set the time and azimuth at the point where the progenitor is disrupted, creating the stream.

We extend these ideas by suggesting that the stream stars with different energies approximately follow a series of geometrically similar orbits, differing only in their time *and length* scales. The orbits of the stream particles predominantly sample radii in the range $5 < r < 150$ kpc. Over this range, our best-fitting model potential for M31 is fairly close to a power law: $\Phi \propto r^k$ with index $k = -0.4 \pm 0.2$, significantly steeper than an isothermal halo. Then we can use the concept of mechanical similarity (Landau & Lifschitz 1976) to relate different orbits that are similar in shape. Let the orbital time scale of such an orbit be proportional to a time scaling factor τ , with $\tau = 1$ for the orbit of the progenitor. Then the radius scales as $\tau^{2/(2-k)}$, the velocity scales as $\tau^{k/(2-k)}$, and the energy scales as $\tau^{2k/(2-k)}$, while the kinetic energy T and total energy E relate as $T = kE/(k+2)$. To derive the phase space position of the stream, we consider a sequence of values of τ . Let us choose the zero-point of time t to be the pericentric passage where the stars are disrupted. (Our model explicitly assumes that the disruption is due to passage near M31, as opposed to some other cause such as an interaction with another satellite galaxy.) Given the orbital position $\vec{r}_p(t)$ and velocity $\vec{v}_p(t)$ of the progenitor, we find the position of a stream star with orbital scale factor τ as $\vec{r} = \tau^{2/(2-k)}\vec{r}_p(t/\tau)$, and the velocity as $\vec{v} = \tau^{k/(2-k)}\vec{v}_p(t/\tau)$. The tilt of the stream in phase space is then just a function of the time past pericenter. (If several streams exist from successive pericentric passages, the temporal zero-point is different for each, implying a different scaling factor τ for each at any given azimuth as well.) The extent of the stream, in contrast, depends on the *spread* in τ or equivalently in orbital energy. This spread depends on the satellite mass as well as its orbit, so we postpone detailed consideration of the stream extent to the next section. With our model, the different orbits do not originate from precisely the same location, but the difference in starting location is smaller than the size of the progenitor itself so this is not a significant problem.

To check this approximate model, we evolve an N-body model of the stream. We assume that the progenitor of the stream is a dwarf galaxy with total mass $2 \times 10^8 M_\odot$, consistent with the mass estimates from the dynamical properties of the stream of Font et al. (2005). We represent the satellite by a Plummer model, and take its scale radius to be 0.3 kpc (note the half-mass radius of a Plummer model is ≈ 1.3 scale radii).

We use $N = 32768$ particles in the satellite, with spline softening length $\epsilon = 30$ pc; only about 0.1% of the mass is contained within one softening length of the center, indicating the satellite is well resolved. We initialize the particle distribution with the ZENO package of J. Barnes; the particle velocities are set by solving an Abel integral for the energy distribution (see Binney & Tremaine 1987), giving an initial configuration very close to equilibrium. We evolved this satellite in isolation for 2 Gyr, and found only negligible changes in the structure of the satellite.

We place the satellite on an inbound orbit on the near side of M31. We take this to be the first approach of the satellite. In reality, unless the progenitor orbit consists of an extremely lucky shot, dynamical friction must be invoked to bring the satellite in to this point.

We perform the calculation with the versatile parallel tree N-body code PKDGRAV (Stadel 2001; Wadsley, Stadel, & Quinn 2004). Our runs use the same fixed Hernquist bulge, flattened exponential disk, and Navarro-Frenk-White (NFW) halo potentials as in our orbit integration code above. The gravity tree uses an opening angle $\theta = 0.8$ and the node forces are expanded to hexadecapole

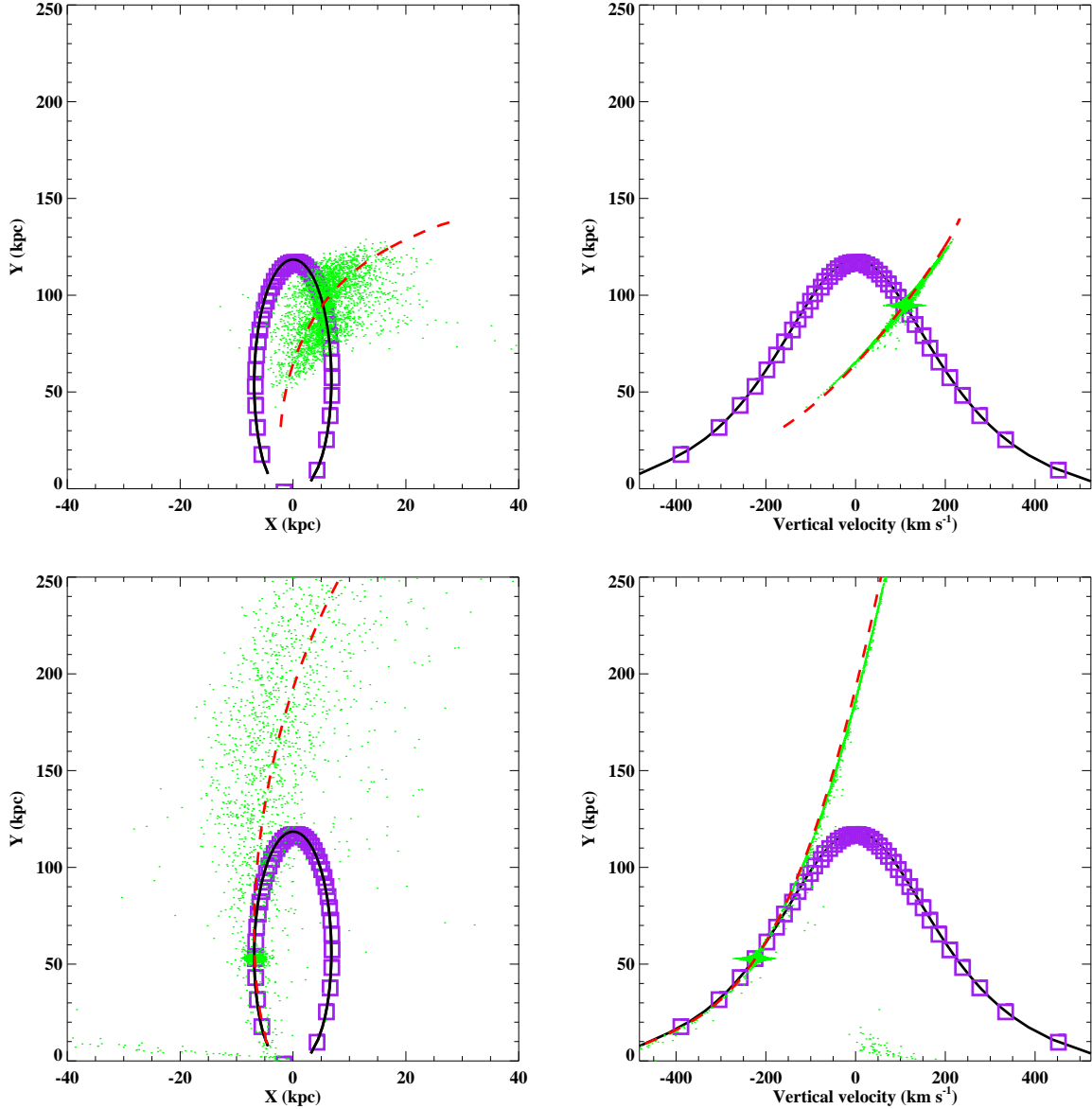


Figure 2. Test of the accuracy of our approximation for the position of the stream in phase space. In these panels, green dots show the particles in our N-body simulation of § 2.2, which uses our best fit to the southern stream data *neglecting* the stream-orbit tilt. The solid line shows the orbit calculated in this potential. Purple squares show the mean trajectory of the central particles of the satellite in this simulation, which closely follows the orbit. Red dashed lines show our approximation for the position of the stream. We choose the coordinate system for this figure so that the satellite orbit executes a radial loop within the X - Y plane, which thus also contains the stream. (Upper left): Spatial position of the particles, on an outbound portion of the orbit past the first pericentric passage. The axis ratio has been distorted for readability. (Upper right): Same as upper left, except shows the Y velocity on the horizontal axis. (Lower left): Same as upper left, except the satellite is now inbound. (Lower right): Same as lower left, except shows the Y velocity on the horizontal axis.

order, while the individual particle timesteps are limited by the acceleration criterion $\Delta t < \eta(\epsilon/a)^{1/2}$ with $\eta = 0.2$.

In Fig. 2, we demonstrate the accuracy of our approximation for the stream. To display the results more clearly, we choose a coordinate system just for this plot such that the radial loop after the first pericenter lies in the X - Y plane. The plots show the trajectory of a single test particle, and the median trajectory of the initially most-bound particles in the satellite. These nearly overlay each other, as expected; the small difference is due to the dynamical effect of the stripped outer portions on the inner core, as we can verify by decreasing the satellite mass. The upper and lower panels show the positions and velocities of the stream particles at two different time stages. At early times, there is a significant tilt of the stream in space relative to the orbit. Later on, this tilt is less-

ened, but the stream extends further in radius than the calculated orbit. This is a product of the systematic gradient in orbital energy along the stream, where the trailing particles have higher energy (Johnston, Sackett, & Bullock 2001). There is also a pronounced tilt in the space of Y versus v_Y . This relation is extremely tight, since the height reached depends almost entirely on the orbital energy. Phrased another way, the large extent in physical space must be balanced by a small extent in velocity space in order to conserve phase space volume.

Our approximation to the stream’s phase-space location is shown as a dashed line. From here on we assume a potential slope of $k = -0.4$; this is consistent with our power-law fit to the potential, and seems to produce the best results on this plot as well. Note the stream approximation describes only the central ridge of

the stream in phase space, and predicts neither its extent along this ridge nor its width. The stream approximation seems to be fairly accurate. Some deviations are apparent, but in general these are fairly small compared to the width of the stream. The approximation is certainly much better than assuming the stream follows the orbit. In the rest of the N-body simulations in this paper, we generally find good agreement with our stream approximation as well. The agreement worsens slightly as the satellite mass increases, since the self-gravity becomes more important, but it still appears acceptable given the observational errors. The approximation thus satisfies our need for an easy way to model the stream in a fitting routine, avoiding the need for many N-body simulations.

2.4 Fits with stream-orbit tilt

We now repeat the fitting exercise above, incorporating the stream-orbit tilt. This adds an extra parameter, the current phase of the progenitor along the orbit. We express this as a fraction of the *radial period*, i.e., $F_p \equiv t/t_r^{(P)}$, where t is the time since the progenitor went through the stream’s last pericentric passage, and $t_r^{(P)}$ is the radial period of the orbit of the progenitor. (This is not to be confused with the *azimuthal* phase Ψ employed by Johnston 1998 among others, though the two are obviously related.) For a stream star, the orbital phase is instead $F = t/t_r$, with t_r the radial period of the particular star. The time scaling factor is then conveniently given by $\tau = t_r/t_r^{(P)} = F_p/F$. We keep $y(0)$ fixed, so we now have eight free parameters: six orbital parameters, plus the halo parameter f_h and the systematic shift Δz in the depth. We test values for F_p ranging from 0.5 to 2.5, or in other words from the apocenter of the stream’s radial loop to the one that is two radial periods ahead. We find F_p is nearly unconstrained by the fit; the changes it introduces in the stream location can be compensated for by changes in the other free parameters. We hence treat it as an external parameter, instead of trying to fit it. For the sake of discussion, we choose $F_p = 1.0$ in this section unless otherwise specified.

When we allow f_h to vary freely, *without* the inclusion of the galaxy fit term in χ^2 , we find best fit values of $f_h \gtrsim 4$ or $r_h \gtrsim 40$. This is not only strongly disfavored by our galaxy fits but implies a halo concentration $C_{200} \lesssim 7$, which is at the bounds of physical plausibility (see Paper I). This f_h value is higher than that in § 2.2, because the gradient of orbital energy along the stream adds to the required potential gradient. However, once we add the term from the galaxy fit, we find a best fit of $f_h \approx 1.2 \pm 0.4$ practically independent of F_p , similar to the results in § 2.2. This implies a mass $M_{125} = (7.4 \pm 1.2) \times 10^{11} M_\odot$. The best fit orbital parameters for several choices of F_p are listed in Table 2 (orbits 2, 3 and 4). The reason for the lowering of f_h from $\gtrsim 4$ to ≈ 1.2 is that the variation in galactic χ^2 dominates the variation from the stream. This is partly because the fit has another way to increase the computed potential gradient besides changing f_h : Δz is set to a lower value, placing the near end of the stream at a smaller distance from M31. Recall that the systematic error in the depth is 16 kpc, compared to the error in the transverse position of about 2 kpc. We are roughly looking down the stream, so the distance uncertainty allows a large shift in the radius and thus in the potential.

Even though the best-fitting f_h is about the same as in § 2.2, the orbit is only about half as long as before; the radial period is 0.80 Gyr, apocenter is at 63 kpc, and pericenter is at 2.7 kpc. The stream-orbit tilt helps to explain why the stream is so strongly radial; the initial conditions required to produce large apocenter-pericenter ratios are rather less special than for an orbit that follows

the stream. The apocenter and radial period decrease with F_p , since it controls the relative sizes of the stream and the progenitor orbit through the scaling factor τ . For example, with $F_p = 1.5$, the best-fitting orbit has radial period 0.56 Gyr, apocenter 46 kpc, and pericenter 2.4 kpc. The period varies only slightly with f_h . Typically, the projection of the second lobe on the sky lies at a smaller position angle, or northward of the NE side rather than eastward as in § 2.2, but the direction is sensitive to exactly where the orbit passes through the disk.

Using our best-fitting orbital parameters (with $F_p = 1.0$), we now repeat our N-body simulation. In this case we doubled the satellite mass to $4 \times 10^8 M_\odot$ and raised the satellite scale radius to 0.6 kpc, to get a better match to the length of the stream, and set the softening length to 0.1 of the new scale radius. We again start the satellite inbound towards the last pericentric passage of the stream; the initial conditions for this point are given as “2e” in Table 2. Fig. 3 compares our orbit and the resulting stream to the observations. The agreement of the observations with the stream approximation is excellent. The agreement with the N-body results is not quite as good, since as in Fig. 2 the approximation slightly underestimates the azimuthal phase of the particles near pericenter, but this offset is comparable to the observational errors. As expected, the progenitor has a more compact orbit than the stream stars; the orbit turns around at about 2.5° , even though the stream itself extends out to 4.5° . With the chosen $F_p = 1.0$, the satellite lies against the M31 disk where it may have escaped detection.

The stream’s continuation on the opposite side of M31 is beginning to develop a shell feature in Fig. 3. This feature is not always apparent; it depends on the orbit orientation and orbital phase. The continuation of the stream is also significantly rotated to the north compared to Fig. 1. After the first pericentric passage, the tidally stripped debris gradually spreads out along the orbit, forming a well-defined stream. After the second passage, the stream acquires a significant width as well. This supports the idea that the narrow southern stream was indeed disrupted less than one radial period ago. The debris forward of the satellite is significantly displaced from the position of the orbit, just like the trailing debris. This effect should be taken into account when trying to match up possible stream orbits with the faint features in the M31 disk.

3 STREAM AND PROGENITOR PROPERTIES

In the previous section, we have considered the properties of the stream that have a direct bearing on the orbital parameters. We have obtained estimates of the orbit of the progenitor, but the orbital phase of the progenitor is unconstrained by the fit and introduces an unwelcome degree of uncertainty to the orbit itself. We also found that the position of the next orbital loop could point in a variety of directions, depending sensitively on the orbital parameters. So before we try to match the orbit to various observed features, let us consider what we can learn about the orbital phase and other properties of the progenitor from stream properties such as its length, width, velocity dispersion, and luminosity. These results should stand up regardless of the identification of the progenitor.

We begin by generating an extended sample of N-body simulations. We use three different orbits, namely 2e, 3e, and 4e in Table 2 which are the best fits for $F_p = 1.0, 1.5,$ and 2.0 respectively. We again select a point on the inbound loop before pericenter as a starting point for each simulation. For each orbit, we test several values of the satellite mass. We adjust the scale length of the satellite along with its mass to keep the characteristic density constant, ensuring similar amounts of satellite disruption in

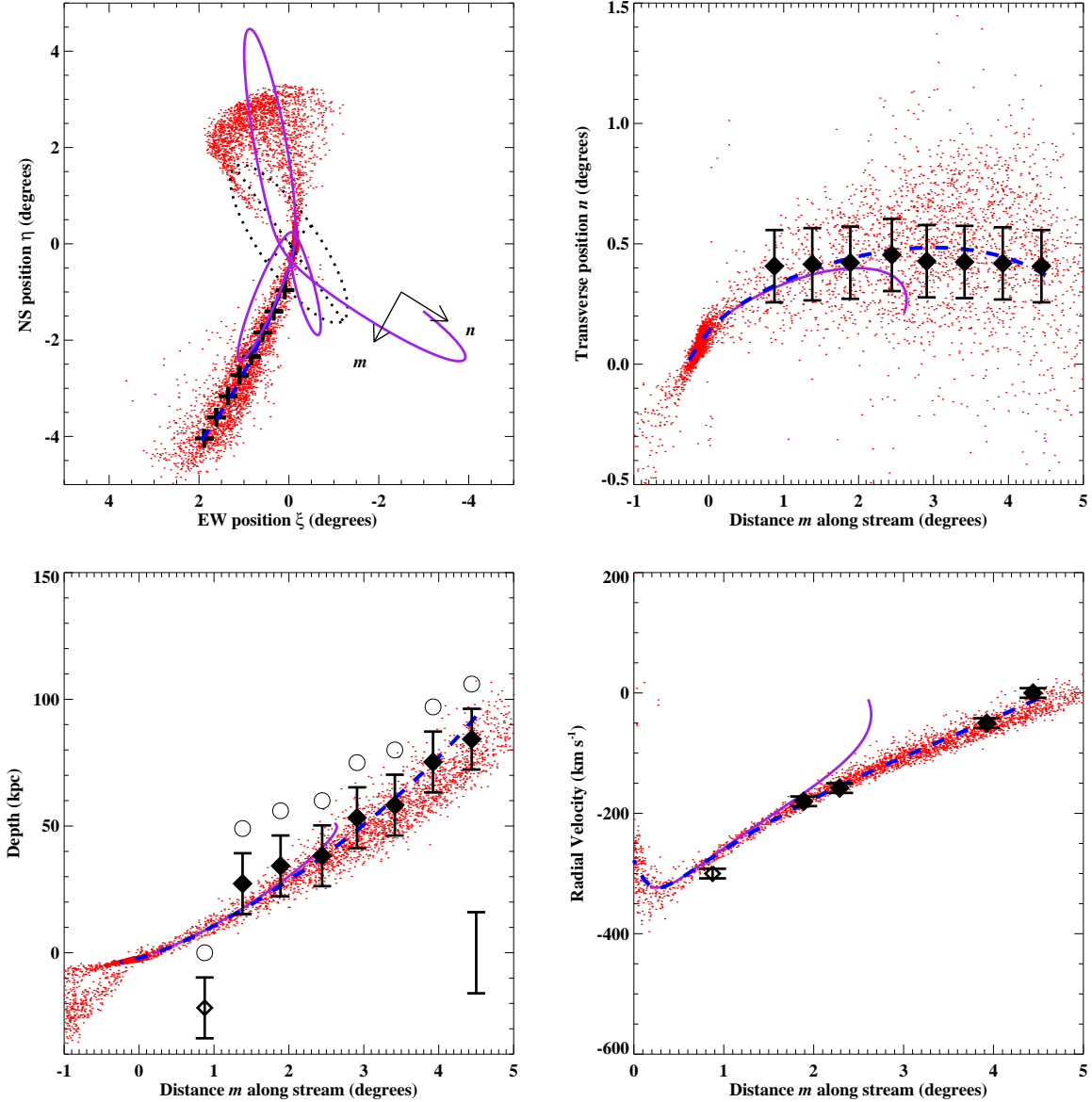


Figure 3. Results accounting for a tilt between the stream and the orbit. Quantities shown in the panels are the same as in Fig. 1. The orbit is shown with purple lines. The corresponding position of the stream calculated using our analytic approximation is shown with blue dashed lines. We conduct an N-body simulation using initial conditions taken from this orbit; particles in this simulation are shown with red points. Observational results are shown with black symbols. The remnant of the progenitor is a small clump near the center of M31, in keeping with the orbital phase of $F_p = 1.0$.

each run. The relation between the mass and velocity dispersion in these runs is consistent with that observed in dwarf galaxies (e.g., De Rijcke et al. 2005), suggesting this characteristic density is reasonable. In all other respects, the simulations are like those described before. The runs and some statistics derived from them are listed in Table 3. The run already displayed in Fig. 3 is “run11” in this table.

We examine the resulting particle distributions at the timestep determined by F_p . One trend is obvious, from the positions of the particles in phase space: as the progenitor mass increases at a fixed orbit, the length, width, and velocity dispersion of the stream increase significantly. This suggests we can obtain an estimate of the progenitor mass by considering these properties of the stream. This work follows up the ideas in Font et al. (2005), but we improve the results by using our revised orbits and some modified formulae, and checking the results with our N-body simulations.

3.1 Length and stellar mass of the stream

The length of the stream is related directly to the spread of energies of its stars. For a satellite of mass M_s and pericenter R_s in an isothermal halo, Johnston (1998) found the energy range of tidal debris tends to be spread out over the range $-2\epsilon < \Delta E < 2\epsilon$, where $\epsilon = V_c^2 (GM_s/V_c^2 R_{peri})^{1/3}$, M_s is the satellite mass, R_{peri} is the pericentric distance, and V_c is the circular velocity at pericenter. By examining our small sample of N-body simulations, we find results consistent with the mass scaling in this formula. However, we find a somewhat smaller spread: in our runs, 97% of the particles have $\Delta E \lesssim 1.3\epsilon$ after the first close pass. (ΔE is distributed roughly symmetrically around 0, but we use a one-sided test here since in some simulation outputs the forward stream is affected by a second pass through pericenter.) Aside from this change, the derivation of Font et al. (2005) for the length of the stream may not

Table 3. Parameters of the N-body simulations used to estimate the stream quantities. Each run is labeled by an arbitrary integer. The orbital phase of the progenitor is denoted by F_p , and the initial conditions corresponding to the orbit label are listed in Table 2. M_s is the total initial satellite mass, and a_s is the scale length of the Plummer model. In each case we take the softening length to be $0.1a_s$. The stream mass M_{stream} is defined as the total mass of N-body particles within the phase space region outlined by Equations 8–11. The fraction of stars in the southern stream still moving radially outward is given by $f_{outbound}$. The values for the angular FWHM of the stream are derived from Gaussian fits with variable baselines; the value marked with a question mark differs significantly from the true width of the stream, owing to the mismatch between the narrow field and the large true width. Finally, σ_{vr} gives the rms dispersion in the velocity relative to the observer of the stars in the stream region, computed by binning the particles as in Fig. 7 and subtracting the mean velocity within the bin before finding the total dispersion.

Run	F_p	M_s ($10^8 M_\odot$)	a_s (kpc)	Orbit	M_{stream} ($10^8 M_\odot$)	$f_{outbound}$	FWHM ($^\circ$)	σ_{vr} (km s^{-1})
13	1.0	0.5	0.3	2e	0.15	0.000	0.26	11
11	1.0	4.0	0.6	2e	1.0	0.021	0.53	14
14	1.0	10	0.815	2e	1.9	0.067	0.69	17
12	1.0	32	1.2	2e	3.5	0.149	0.91	25
23	1.5	0.5	0.3	3e	0.0003	0.000	0.11	5
21	1.5	4.0	0.6	3e	0.33	0.000	0.32	12
24	1.5	10	0.815	3e	1.6	0.008	0.55	16
22	1.5	32	1.2	3e	4.1	0.078	0.39?	24
34	2.0	10	0.815	4e	0.38	0.003	0.34	14
32	2.0	32	1.2	4e	3.2	0.030	0.86	22

be valid for large energy spreads or for non-isothermal halos. We hence derive the relation as follows.

Our mechanical similarity argument in § 2.2 implies that the orbital energy $E = E_0 + \Delta E$ depends on the time scaling factor τ as $E/E_0 = 1 - \Delta E/|E_0| = \tau^{2k/(2-k)} \approx \tau^{-1/3}$. (The energy E_0 of the progenitor is negative, if we are using the approximate power-law form for the potential; hence τ increases with ΔE). We then find

$$M_s = \frac{R_{peri} |E_0|^3}{1.3^3 G V_c^4} (1 - \tau_{max}^{-1/3})^3. \quad (5)$$

Here τ_{max} is the value of the time scaling factor at the end of the stream, and equals the ratio of the orbital phase of the progenitor F_p to that of the stream stars at stream end. In our case we know that the stream extends just about to apocenter where the phase $F = 0.5$, so $\tau_{max} \approx 2F_p$. We obtain R_{peri} and E_0 from the orbit of the progenitor, and we take $V_c = 250 \text{ km s}^{-1}$.

We can also derive a constraint on the mass from the other end of the southern stream, Field 8 of McConnachie et al. (2003) which is the closest field to M31 and the furthest along in the orbit. Since this field does not necessarily represent the end of the stream, we can only derive a *minimum* satellite mass, valid when the progenitor is assumed to lie within the visible extent of the stream:

$$M_s > \frac{R_{peri} |E_0|^3}{1.3^3 G V_c^4} (\tau_{F8}^{-1/3} - 1)^3. \quad (6)$$

We obtain τ_{F8} by matching the m coordinate of Field 8 to the calculated m coordinate of the stream as a function of τ .

We can now estimate the satellite mass required to produce the visible extent of the stream. We use the best fit parameters evaluated for a series of F_p , restricting the value of f_h to the values 1.2 (our best fit for most values of F_p) or 2.0 ($\sim 2\sigma$ higher). The preferred mass from Equation 5 is shown as the black lines in Fig. 4. The estimates from the two values of f_h do not differ too much, indicating our result for the required progenitor mass is fairly robust. The main thing to observe is the strong correlation between the orbital phase and the mass. The primary reason for this is the dependence on F_p through τ_{max} . As the orbital phase increases for a *fixed* orbit, the value of the mass must increase in order to create a

stream out to apocenter. There are also changes in the orbital quantities E_0 and R_{peri} as the best-fitting orbit changes as a function of F_p , but these are smaller effects and nearly cancel out in any case. The minimum satellite mass from the forward extension in Equation 6 is also shown in the plot. This places only a weak limit on the mass and orbital phase, which will shortly be superseded.

The estimate of the satellite mass from the stream length has significant uncertainty, since we are relying on an analytic scaling relation which has not been rigorously established. Also, the “end” of the stream is not very precisely defined; since the energy distribution of stream stars drops off rapidly but continuously with ΔE , if the observationally apparent end of the stream extends to apocenter, there should be a small fraction of stars ($\sim 3\%$) that are still moving outwards towards apocenter. We can test the formula with our N-body simulations. Table 3 lists the fraction of the total stars moving outwards; this is clearly a very steep function of the progenitor mass for a given orbital phase. If we require this fraction to be 3% of the total stars in the progenitor, and interpolate the results in the table, we obtain an estimate of the progenitor mass. (This mass is not very sensitive to the adopted threshold, since the number of stars at large ΔE is falling rapidly with E). These estimates, shown as filled circles in Fig. 4, seem to be consistent with Equation 5. This is not too surprising, since we used these runs to calibrate the numerical constant in this equation, but it is reassuring nevertheless.

The stellar luminosity in the stream gives us an alternate means of estimating the progenitor mass. The red dashed line in Fig. 4 shows the estimated stellar mass $M_{stream} \sim 2.4 \times 10^8 M_\odot$ of the stream (Ibata et al. 2001a). Allowing for dark matter, this gives a lower limit on the total mass. This immediately produces a tighter limit on the mass and orbital phase than the length of the stream alone. However, the fraction of stars that lie within the stream region can be quite small, and varies strongly with the mass and orbital phase. For the sake of argument, let us assume that the energy of the stream stars is distributed uniformly in the range $-1.3\epsilon < \Delta E < 1.3\epsilon$. We can use this to derive the fraction of stars that lie within the allowed range $\tau_{F8} < \tau < \tau_{max}$. In turn, this raises the estimate of the mass of the progenitor to

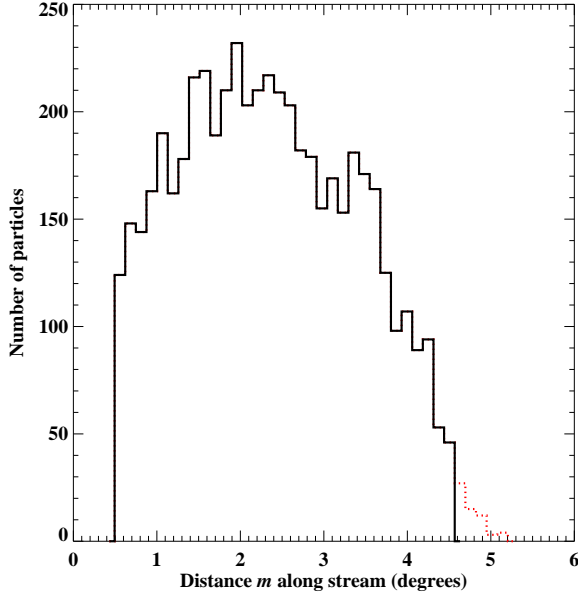


Figure 5. Shows the distribution of N-body particles along the stream, using run 24. Position m along the stream is defined the same way as in Fig. 3 (so its sign is reversed from Fig. 4 of McConnachie et al. 2003). Cuts are made to the sample as described in the text. The dotted line continues the histogram without the sample cut in Equation 8.

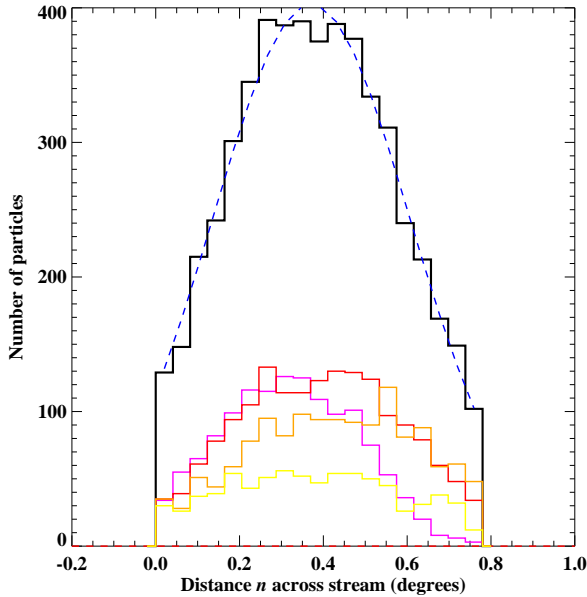


Figure 6. Shows the distribution of N-body particles as a function of n , the coordinate direction perpendicular to the stream, using run 24. Position n across the stream is defined the same way as in Fig. 3 (so the sign is reversed compared to fig. 3 of McConnachie et al. 2003). The NE side of the stream is to the left. Cuts are made to the sample as described in the text. The low-amplitude magenta, red, orange, and yellow histograms (highest to lowest at the peak) show the distribution in quadrants of increasing distance along the stream, while the black histogram shows the total. The blue dashed curve shows a Gaussian fit with a variable baseline, having FWHM 0.57° .

If the stream is too long, the histogram will rise towards its end; whereas if the stream is too short, it will cut off in the middle of its range. To the limited extent we can tell, given the background issue, the distributions appear to agree quite well. This again indicates our progenitor mass and pericenter are reasonable.

In Fig. 6, we display the distribution of N-body particles in the direction normal to the stream. This can be compared to fig. 3 of McConnachie et al. (2003), though again that figure contains background stars not present in our run. The stream in our run happens to be centered in our chosen selection region (the observed stream is slightly offset from the selection region used here). We find the rise in the number on the NE side is comparable to that in the observed stream (the other side is cut off by the field boundary in the observations). However, some outlier particles are present in non-Gaussian tails outside the width of the fields, as can be seen in the top panels of Fig. 3. Stars showing this behavior would probably fade into the general halo population in surveys using number counts alone. In fact, it is possible that they make some contribution to the wide-field, minor-axis photometric surveys of Durrell, Harris, & Pritchett (2001, 2004). These fields are far enough away from the stream that, in our “run24”, $\lesssim 5 \times 10^5 M_\odot$ of stream material is covered by the two fields in this survey. From the relative surface brightnesses in the stream and in the survey fields, we estimate this represents only a few percent of the total mass of halo stars in these fields. However, this contamination would be very sensitive to the orbit, size, and radial mass profile of the incoming progenitor, so we cannot rule out the possibility that it contributes significantly to the observed population in these surveys. Interestingly, these surveys found a metallicity distribution peaking at $[m/H] \sim -0.5$, similar to the metallicity of the stream. In general, these outlier stars will share in the distance and velocity signature of the stream, so they may be recognizable in spectroscopic surveys.

Font et al. (2005) suggested that the spatial width of the stream (defined to contain 80% of the stream luminosity, which for a Gaussian is the FWHM) at a physical distance R from M31 could be expressed as $w = sR$, where $s \equiv (GM_s/V_c^2 R_{peri})^{1/3}$. Using this estimate, they fitted a Gaussian with a floating baseline to the transverse distribution of the stream stars and inferred $M_s \approx 1.3 \times 10^8 M_\odot$; this is quite low compared to their estimate from the stellar metallicity. Font et al. dismissed this discrepancy, noting that if the progenitor was partially supported by rotation it might reduce the width of the stream.

We mimic their procedure by fitting a Gaussian with an arbitrary baseline to the N-body runs. The resulting estimate for the FWHM is given in Table 3, which shows that it increases systematically with M_s . We find that this is not a completely robust procedure to recover the true width of the stream, because the window is narrow and the non-Gaussian tails can masquerade as a baseline. Nevertheless, in most cases we recover nearly the same answer as we would with twice as wide a window, so their width measurement is probably accurate. Font et al.’s analytic formula systematically overpredicts the estimated width in our runs. However, if we multiply their formula for w by 0.4, we get fairly good agreement overall. It may be that their formula simply needs this scaling constant, which raises the mass at a given width by more than an order of magnitude, although more thorough testing of this is warranted. The best agreement of our N-body runs with the observed width is obtained for $M_s \sim 10^9 M_\odot$, consistent with our other estimates. The mass estimated this way is not very precise but is probably good to a factor 3. If we interpolate the results in Table 3 to find the FWHM at a stream mass of $M_{stream} = 2 \times 10^8 M_\odot$, as we did with the mass earlier, we find results of 0.71° , 0.50° , and 0.70° for $F_p = 1.0, 1.5,$ and 2.0 respectively. Although the precision of

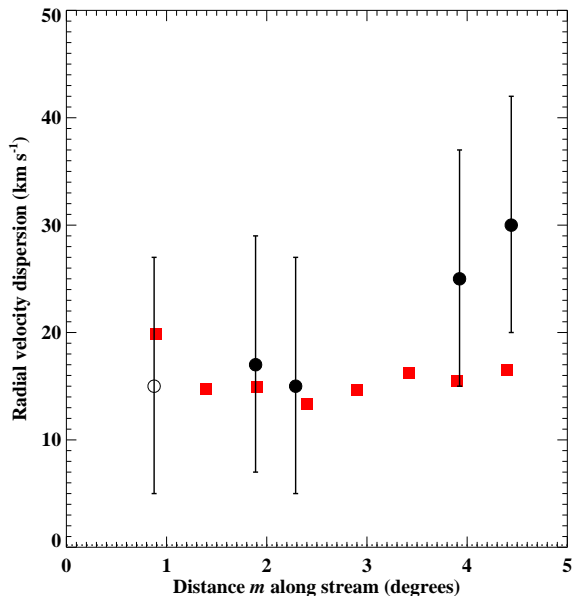


Figure 7. Shows the line-of-sight velocity dispersion of N-body particles in run 24 (red squares), as a function of position m along the stream. The points are computed by taking particles within the stream region (Equations 8–11), binning them in m , and finding the standard deviation of the velocity of the particles in each bin. Black circles with error bars show the observed velocity dispersion in five fields from Guhathakurta et al. (2005) and Ferguson et al. (2004). We indicate the field in Ferguson et al. closest to M31 with an empty symbol due to its potential contamination with the disk. A rough error bar of 10 km s^{-1} is assumed for each observed point.

these estimates is low, they indicate that models that reproduce the stream *mass* also reproduce the stream *width* fairly well, independent of the orbital phase.

Fig. 7 shows the rms velocity dispersion at several points along the stream. Observed values of the velocity dispersion are shown in the figure as well; these are quite uncertain, given the small number of stars and the possibility of contamination by additional structure in the background density. The dispersion in the N-body model is certainly consistent with the observations, suggesting our progenitor mass is roughly correct.

Font et al. (2005) suggested $M_s \gtrsim 2.0 \times 10^8 M_\odot$ from the velocity dispersion; they noted that this is a lower limit since the observed portions of the stream may be dynamically colder than the progenitor itself, which we indeed find to be the case (cf. the right-hand panels of Fig. 2). We find the central velocity dispersion of the progenitor is $\sim 25 \text{ km s}^{-1}$, while the *M31-centric* radial velocity dispersion as a function of *M31-centric* radius drops to very low values ($\lesssim 5 \text{ km s}^{-1}$) throughout the stream. The larger line-of-sight dispersion in Fig. 7 is primarily due to the fact that the stream stars form a fattened, tilted tube in three dimensions, and thus a single line of sight probes particles at a range in *M31-centric* radius which depends on the tube’s thickness. As a result, there is a good correlation between the transverse width and the velocity dispersion in Table 3.

Font et al. also suggested that the velocity dispersion, should increase sharply near apocenter. In contrast, Fig. 7 shows it to be roughly constant to the last measured point, at nearly the end of the stream. The difference may arise from Font et al.’s use of azimuthal binning rather than our binning in transverse position m . It is difficult to compare our results directly, as the stream particles in our

runs occupy only a small range in azimuth, blurring any correlation that might exist.

If we again interpolate the results in Table 3, this time to find the velocity dispersion at a stream mass of $M_{stream} = 2 \times 10^8 M_\odot$, we find results of 18, 18, and 20 km s^{-1} for $F_p = 1.0$, 1.5, and 2.0 respectively. Again, there does not seem to be a strong trend with orbital phase for a *fixed* mass of stars in the stream.

In summary, we find that the various observed properties of the stream give consistent indications of the mass. Our simulation with a mass of $M_s = 10^9 M_\odot$ and an orbital phase of $F_p = 1.5$ is the one that is most consistent with the observed properties of the stream. There is some leeway in these quantities, however, as long as the mass and orbital phase increase together in keeping with Fig. 4. Aside from detection of the progenitor itself, radial velocity surveys will probably be the most powerful tool to constrain the progenitor mass. Radial velocity surveys to a greater transverse extent may help to differentiate between unrelated halo stars and the sideways extension of the stream, which would give additional constraints on the properties of the progenitor.

4 FORWARD CONTINUATION OF THE STREAM

From the analysis in the previous section, we now have a better idea of the mass and orbital phase of the progenitor. We now consider the continuation of the stream past the next pericenter. For the fit shown in Fig. 3, the second lobe projects about 30° counter-clockwise of M31’s NE major axis, but this direction is sensitive to the orbital parameters. If we impose further observational constraints, this loop can point in a variety of directions which encompass a number of faint features observed near M31. As photometric and velocity surveys go deeper and deeper, more faint features will probably continue to turn up, and it is quite possible that the progenitor is not even a currently identified feature. Nevertheless, it is worth testing which of the currently identified features can be the progenitor.

Table 4 gives the observational data for a number of these features in the disk and inner halo regions of M31. We perform fits in the same manner as in § 2.4, but we add further data points for the sky position of the progenitor, and its depth or radial velocity if these are known. Most of these possible progenitors require a phase $F_p > 1.0$. Once the progenitor passes through pericenter for a second time, a second stream develops, which again does not follow the orbit. However, in our N-body simulations, the progenitor itself follows the calculated orbit fairly closely, though there are some slight deviations due to the self-gravity of the satellite matter. The position and velocity of the stream thus can be derived directly from the calculated orbit and the orbital phase F_p .

The errors on the observational data are in many cases not well specified, so we have chosen reasonable values in order to perform the fit. For example, some of the features are not very well-defined spatially, including the Northern Spur, the Merrett et al. planetary nebulae (PNe), and the Eastern Shelf. We assume positional errors of $0.05\text{--}0.2^\circ$, depending on how well-defined the object is. In Table 4, if the distance or velocity are not known for a particular feature, we supply the results from our fit in brackets. In some cases there may be alternate solutions to the one we have computed, where the progenitor has a different orbital phase, especially if only the sky coordinate of the feature is known. We now discuss the suitability of the following features as progenitors.

Linear continuation: McConnachie et al. (2003) observed two fields along the linear projection of the southern stream on the other side of the disk. Even though there is no obvious projection seen in

Table 4. Kinematic data and predictions for possible progenitors of the stream. Brackets indicate that the field is a prediction from our best-fitting orbit, as opposed to observational data. d' and v_r' give the radial displacement and velocity relative to M31. The depth offset Δz and orbital phase F_p are taken from our fit. The final entry gives the value of reduced χ^2 from our fit. The number of degrees of freedom in each case is 13 plus the number of observational constraints in the table.

Field/Name	ξ (deg)	η (deg)	d' (kpc)	Δz (kpc)	v_r' (km s $^{-1}$)	F_p	χ^2/N_{deg}
Linear continuation	-1.0 ± 0.2	$+1.3 \pm 0.2$	-35 ± 12	-13	[-70]	1.1	1.8
NGC 205	-0.5 ± 0.05	$+0.4 \pm 0.05$	50 ± 12	—	$+55 \pm 10$	—	—
M32	$+0.0 \pm 0.05$	-0.4 ± 0.05	0 ± 12	-15	$+100 \pm 10$	2.0	1.0
Merrett NE PNe	$+1.0 \pm 0.2$	$+1.4 \pm 0.2$	[-40]	-6	-190 ± 10	1.1	0.8
Northern Spur	$+0.7 \pm 0.2$	$+1.8 \pm 0.2$	[-21]	-13	[-127]	1.1	0.6
Northern Spur, v constraint	$+0.7 \pm 0.2$	$+1.8 \pm 0.2$	[-12]	-13	200 ± 30	1.8	1.3
And NE	$+1.2 \pm 0.1$	$+3.0 \pm 0.1$	[-21]	-16	[14]	1.5	0.5
Eastern Shelf	$+1.8 \pm 0.2$	$+0.6 \pm 0.2$	[-56]	8	[-92]	1.3	1.3
And VIII	$+0.1 \pm 0.2$	-0.7 ± 0.2	[-53]	15	-205 ± 20	1.2	2.1

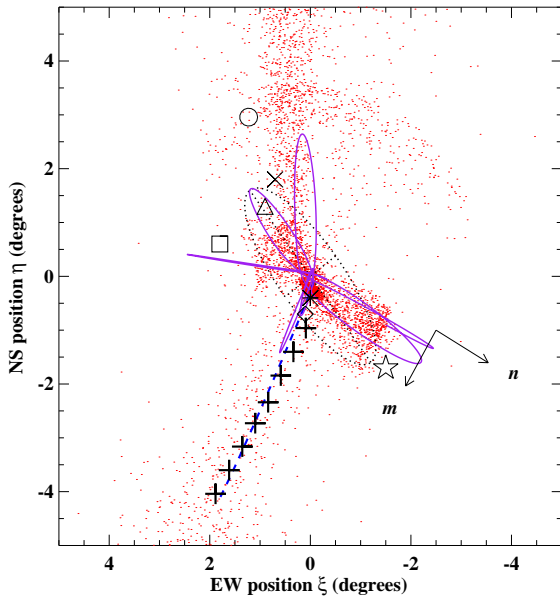


Figure 8. Best-fitting orbit passing through M32, and the particle distribution in the corresponding N-body simulation. Crosses, orbits, and dots have the same meaning as in Fig. 3. The particles corresponding to M32 itself are barely visible in this plot as the clump just south of the center of M31. The point density in the stream is smaller than in Fig. 3, because we use a larger particle mass in this run to match the larger mass of the progenitor. Observed positions of some of the faint features are plotted as symbols: Northern Spur (cross), And NE (circle), eastern Merrett PNe (triangle), the Eastern Shelf (square), M32 (star), And VIII (diamond), and the G1 clump (star).

surface brightness maps, they obtained red giant color-magnitude diagrams for these fields consistent with a stream component. We assign a position to this feature using the center of Field 13 and errors of 0.2° . Since the projected orbit tends to bend substantially at pericenter, we find it is very difficult to fit this feature as the progenitor itself, in agreement with the conclusions of Ibata et al. (2004) and Font et al. (2005). However, it is possible that the stream scatters enough debris to the side when it passes through pericenter to produce the stars seen by McConnachie et al.

NGC 205 and nearby arc: NGC 205 is close to the projection of the stream to the other side of M31. However, its velocity has the opposite sign from that of the stream. If it is the progenitor, it must lie nearly at the *next* pericenter, i.e. at phase $F_p \sim 2.0$. Because of its location north of M31, it is difficult to fit an orbit

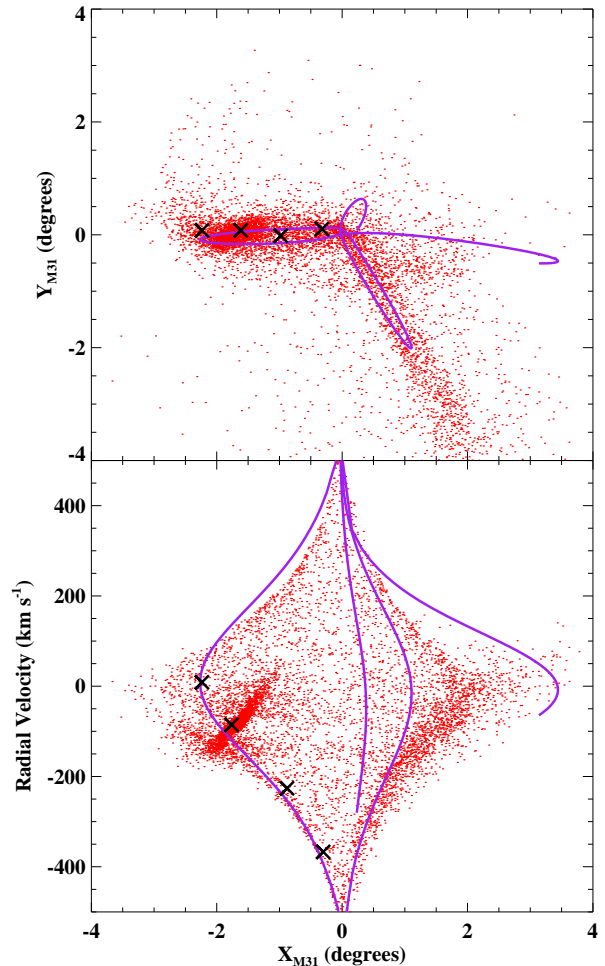


Figure 9. Best-fitting orbit passing through the Merrett et al. (2003, 2004) PNe. In this plot we have changed to their M31-aligned coordinate system to allow easier comparison with their figures. X_{M31} increases along M31's major axis to the SW, and Y_{M31} along its minor axis to the NE. The four crosses in each panel show approximate points along the narrow-velocity-dispersion group of PNe identified in Merrett et al. (2004).

with this constraint. The stellar arc through the center of NGC 205 (McConnachie et al. 2004) produces the same difficulties with the orbit as NGC 205 itself. In addition, the bluer color of the red giants in NGC 205 and the arc indicate a lower metallicity compared to the stream, again arguing against a connection with the stream.

M32: M31’s other prominent nearby satellite galaxy is an obvious candidate for the origin of the stream, and was proposed as such as soon as the stream was discovered (Ibata et al. 2001a). M32 lies almost directly on the path of the stream. However, as with NGC 205, its radial velocity has the wrong sign for it to lie within the southern stream. Hence it too would have to be at the next pericenter ($F_p \sim 2.0$). Interestingly, on orbital grounds alone, it is not possible to rule out this possibility. We find an acceptable fit, even though the observational constraints on this fit are more numerous and more precise than for any other candidate (since the position, distance, and radial velocity are all fairly well known). The angle of the second loop in this fit is not very robust, and could accommodate a wide range of position angles ranging from 0 to 60° , which encompasses a range of observed structures, although the best-fitting orbit, shown in Fig. 8, does not result in an obvious match to any in particular. The progenitor mass before last pericenter required to produce the length of the stream is about $M_s = 2.5 \times 10^9 M_\odot$. However, it then must lose much of its mass to the forward and backward streams in order to produce the observed luminosity of the stream. Mateo (1998) gives the *current* mass of M32 as $2.1 \times 10^9 M_\odot$. Within the uncertainties, the masses are probably consistent. From studying the isophote ellipticity of M32, Choi, Guhathakurta, & Johnston (2002) inferred that it is on a highly eccentric orbit with $R_{peri} < 1.7$ kpc, which is consistent with our best-fitting orbit. However, these authors also inferred that M32 is most likely moving eastward; this is not consistent with our orbit, though it is difficult to evaluate the reliability of their argument. There are other difficulties with our specific orbit: it creates a plume in the northward direction that has not been reported observationally, and it is not clear that the stream forward of M32 can match the observed structure. The metallicity distribution of M32 is complex, and it is not clear whether or not it would be consistent with that of the stream. Nevertheless, on balance of the evidence, M32 continues to be a possibility for the progenitor of the stream.

Merrett et al. PNe: Merrett et al. (2003) surveyed the disk of M31 for PNe and found a number that had velocities inconsistent with the disk kinematics. Almost by definition, most of them move in a direction opposite to the local rotation of the disk, though a few move in the same direction but with larger speeds. Merrett et al. (2004) pointed out a subset of these on the northeast side that occupy a narrow region in position-velocity space. We can easily fit this group as the progenitor of the stream. (Merrett et al. also fit an orbit connecting this group to the stream using their simpler potential, but without demonstrating agreement with the detailed properties of the stream.) Choosing the position and velocity to lie within the northeast group, we find an excellent fit with the initial conditions given in Table 2. Fig. 9 shows the positions and velocities obtained from an N-body simulation using this orbit, using a coordinate system aligned along the major axis of M31. These can be compared to fig. 3 of Merrett et al. (2004). Interestingly, there are a significant number of N-body particles occupying larger velocities at a given position than the main concentration, but none with smaller velocities; a similar pattern is seen in Merrett et al. (2004). This feature is thus a prime candidate for the progenitor of the stream.

Northern Spur: The star-count maps of M31 in Ferguson et al. (2002) show a faint clump of stars at the NE end of M31, called the Northern Spur. We estimate the position of the Spur from the

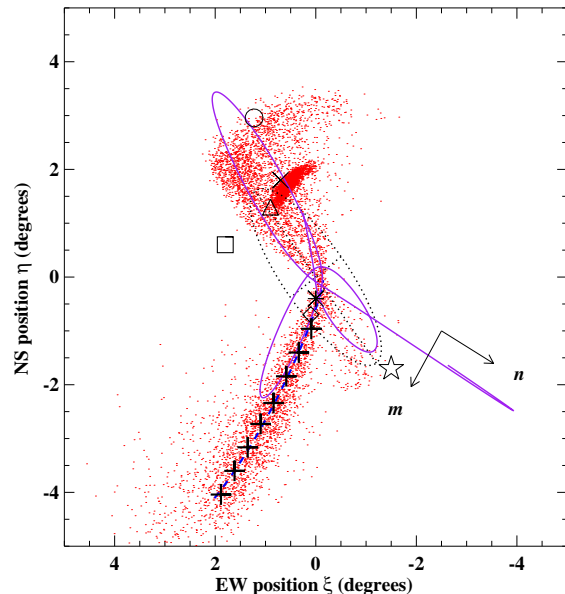


Figure 10. Best-fitting orbit passing through the Northern Spur, and the particle distribution in the corresponding N-body simulation. Crosses, orbits, and dots have the same meaning as in Fig. 3. Object symbols are the same as in Fig. 8. The progenitor is visible as the dense elongated clump near the NE end of M31.

image in Zucker et al. (2004), which also is suggestive of a loop of emission extending from the Spur. The red giant branch color is similar to that of that of the stream (Ferguson et al. 2002). This feature is a prominent candidate for the continuation of the stream (Merrett et al. 2003).

Some radial velocity observations exist in the Spur region. From spectroscopy of red giants, Ferguson et al. (2004) claimed a velocity of $\sim 150 \text{ km s}^{-1}$, significantly different from that of the disk in this region, suggesting it is a distinct object. Merrett et al. (2004) found an overdensity of PNe in this region. The velocities of some of these are consistent with the disk velocity in this region, some have larger velocities, and some have the wrong sign altogether. These authors inferred that the Spur represents a warp in the disk of M31. The possible contamination from the disk and the presence of velocities of both signs suggest that if the progenitor lies in the Spur region, its velocity cannot be reliably constrained at present.

If we impose no velocity constraints, we find an excellent fit to the position of this feature, as seen in Fig. 10. The predicted location is on the near side of M31, and the progenitor is outward bound from pericenter, giving a negative radial velocity. Thus slight differences in its color-magnitude diagram in Ferguson et al. (2002), as compared to that of the stream, could possibly be explained by its smaller distance. One possible problem is the faint luminosity of the Spur; from the area and surface brightness discussed in Ferguson et al. (2002), we estimate its V -band luminosity is only $8 \times 10^6 L_\odot$, less than that of the stream. The simulation shown in the figure produces a fairly dense group of particles at the position of the Spur, and would probably need to be adapted to produce a fainter, lower-surface-brightness core.

If we instead assume that the velocity is positive, as suggested by the majority of the velocity data, the progenitor must be moving inwards once again. In this case it is more difficult to fit a model to the Spur. Our best fit is formally ruled out, though this conclusion

is dependent on the assumed errors for the Spur’s properties (we assume a velocity $200 \pm 30 \text{ km s}^{-1}$ and a positional error of 0.2°).

And NE: This low surface brightness enhancement far out along the major axis of M31 was discussed by Zucker et al. (2004). We find it is quite easy to make the orbit pass through this object. However, this solution is objectionable on other grounds: there is no visible connection to the stream, despite the low surface brightness of M31 at these projected radii, and the luminosity is probably too low for it to be an intact progenitor.

Eastern shelf: Ferguson et al. (2002) discussed a diffuse surface brightness enhancement on the eastern side of M31, which contained high-metallicity red giants judging by their color. This feature is now known as the “Eastern Shelf”. This color may be consistent with that of the Northern Spur and of the stream itself. With the position we have assigned to this feature, it is not easy to find an orbit where this feature is the progenitor itself, despite the weakness of the observational constraints. This conclusion differs from that in Font et al. (2005) because the greater strength of their potential, and their use of an orbit that follows the stream, affect the direction of the second loop. The low surface brightness of this feature also argues against it being the progenitor. It might represent debris from the continuation of the stream, though for none of the orbits we tried did the debris reach the position angle of this feature.

And VIII: This is another group of objects with abnormal radial velocities in the M31 disk (Morrison et al. 2003), in this case a combination of PNe, globular clusters, and H I detections. This feature lies nearly across the stream and has a velocity consistent with it, but it is extended for $\sim 1^\circ$ transverse to the stream, which is not expected for a progenitor moving along the stream. Hence if it is the progenitor, it has probably passed through pericenter already. Incorporating this condition as a constraint, we find that it is very difficult to fit an orbit to this feature.

G1 Clump: Ferguson et al. (2002) identified a diffuse surface brightness enhancement in the vicinity of the globular cluster G1, which they called the “G1 clump”. We did not attempt to fit this as the progenitor of the southern stream. By virtue of its position, this would have to lie at $F_p \approx 2.5$. This would make for a very massive progenitor. The G1 clump, however, is less luminous and thus less massive than the stream, and it is not clear that the progenitor mass in excess of these two structures can be hidden. In addition, the color-magnitude diagram of the clump differs from that of the southern stream. However, it is at least suggestive that in a number of our N-body simulations of other possible progenitors, there is a clump or shell-like feature in roughly the vicinity of this feature, where the forward section of the stream turns around (see Figs. 8 and 10).

In summary, the preferred mass and orbital phase of the progenitor indicate there is probably a significant amount of structure near M31 that is physically connected to the stream but ahead of it in its orbit, amounting to $\gtrsim 10^9 M_\odot$ in total. We can probably rule out most of the objects on the southwestern half of M31 as progenitors, with the possible exception of M32. We can fit reasonable orbits through several features in the northeastern half: the Northern Spur, And NE, and the Merrett et al. PNe. N-body simulations following these orbits produce a spray of debris as well as a number of discrete-looking features; there is some resemblance between this debris and the structure seen in the observations, even though we do not have a detailed match. We have made significant approximations in the fitting and simulation process, among them the neglect of dynamical friction, the assumption of a static fixed

potential, and the neglect of the satellite’s self-gravity in deriving the best-fitting orbit. Thus we have not tried to refine the match to the observed features any further. However, by predicting the distance and velocity of each feature, we hope to speed the process of confirming or rejecting a connection between the various faint features and the southern stream.

5 SUMMARY

In this paper and Paper I, we have attempted to construct a model for the interaction of M31 and the southern stream. We constructed a simple analytic model for the potential, and found its best fit parameters by fitting to a number of observational constraints. We then combined this galaxy fit with a fit to the observed path of the southern stream. We found the best fit parameters as a function of the orbital phase of the progenitor. By considering the effect of the progenitor’s mass on the observed properties of the stream, we derived an N-body model of the interaction that fits current observations reasonably well. We tested the orbital fits against various objects and surface brightness features near M31, ruling out some as the progenitor and making predictions for the kinematic properties of the others.

In comparison to the stream from the Sagittarius dwarf galaxy that surrounds the Milky Way, there is currently much more leeway in fitting the Andromeda stream. The progenitor of the former stream is known, and its proper motion has been measured. Distance errors for this stream are a factor of 10 smaller than for M31. In addition, this stream has been followed for nearly a full circle around the Galaxy, as opposed to the Andromeda stream which spans less than half a radial period. Thus, this stream is currently a much better probe of its parent halo’s properties than in the case of M31 and its southern stream. In this paper, we have found that the orbital phase of the progenitor is a major source of uncertainty in the orbital parameters. If we can identify the progenitor location, we can immediately put much stronger constraints on the orbital properties of the stream. We can then get a better understanding of the mass distribution in M31, calculate the properties of the progenitor satellite, untangle the possible relationships of the various surface brightness features, and perhaps find signatures of the passing satellite in the M31 disk.

Our specific conclusions are as follows:

- The stream follows a path in phase space significantly different from the orbit of the progenitor satellite. Allowing for this effect decreases the estimated apocenter and increases the estimated gravitational force in the M31 halo.
- The narrowness and surface brightness are consistent with a young stream, resulting from the last pericentric passage of its progenitor. Larger ages are ruled out by the narrowness and high luminosity of the stream.
- With the current observational uncertainties, the stream itself does not add much constraining power to the galaxy model. Our best combined fit for the mass of M31 within 125 kpc is $(7.4 \pm 1.2) \times 10^{11} M_\odot$, only slightly larger than in our best-fitting model from Paper I.
- If the progenitor satellite has orbital phase $F_p = 1.0$ (at the next pericenter beyond the stream location), our best fit to the orbit of the progenitor has radial period 0.8 Gyr, apocenter 63 kpc, and pericenter 2.8 kpc. However, F_p , which determines the size and time scales of the orbit, is poorly determined. We find it likely that the satellite or its disrupted remnants lie beyond next pericenter.
- The dynamical mass of the progenitor at the previous pericen-

tric passage was $M_s \approx 10^9 M_\odot$, within a factor 3. Its mass was not heavily dominated by dark matter; otherwise, the surface brightness of the stream would be less than is observed.

- Depending on the exact properties of the progenitor, significant amounts of debris from the progenitor may lie outside the currently observed width of the stream. These stars could contaminate the metallicity distribution measured in off-stream fields, but can be detected since they share the velocity and distance signatures of the stream.

- Most of our orbital fits would place the continuation of the stream past next pericenter and to the NE of M31's center. We can fit reasonable orbits through several observed features, among them the Northern Spur, And NE, M31, and a feature in the planetary nebula distribution found by Merrett et al. The latter feature seems to be the most plausible candidate for the progenitor of the stream.

ACKNOWLEDGMENTS

We thank Tom Quinn, Joachim Stadel, James Wadsley, and Josh Barnes for the use of their simulation and analysis codes. Andreea Font, Kathryn Johnston, Steve Majewski, and Mike Rich graciously conveyed their revised stream model prior to publication. We thank Dave Balam, Chris Pritchett, and Andreea Font for helpful conversations. Research support for JJG, MF and AB comes from the Natural Sciences and Engineering Research Council (Canada) through the Discovery and the Collaborative Research Opportunities grants. AB would also like to acknowledge support from the Leverhulme Trust (UK) in the form of the Leverhulme Visiting Professorship. PG is supported by NSF grant AST-0307966. He is grateful to the HIA/DAO/NRC staff for graciously hosting his 2002-03 Herzberg fellowship during which time this collaborative project was conceived.

REFERENCES

- Binney, J. & Tremaine, S. 1987, "Galactic Dynamics", Princeton University Press, Princeton, NJ
- Choi, P. I., Guhathakurta, P., & Johnston, K. V. 2002, *AJ*, 124, 310
- Durrell, P. R., Harris, W. E., & Pritchett, C. J. 2001, *AJ*, 121, 2557
- Durrell, P. R., Harris, W. E., & Pritchett, C. J. 2004, *AJ*, 128, 260
- Ferguson, A. M. N., Irwin, M. J., Ibata, R. A., Lewis, G. F., & Tanvir, N. R. 2002, *AJ*, 124, 1452
- Ferguson, A., Chapman, S., Ibata, R., Irwin, M., Lewis, G., McConnachie, A. 2004, in Proc. of ESO-Workshop "Planetary Nebulae beyond the Milky Way", eds. J. R. Walsh, L. Stanghellini, Springer-Verlag (astro-ph/0408058)
- Font, A., Johnston, K. V., Guhathakurta, P., Majewski, S. R., & Rich, R. M. 2005, *AJ*, in press (astro-ph/0406146)
- Geehan, J. J., Fardal, M. A., Babul, A., Guhathakurta, P. 2005, *MNRAS*, in press (Paper I)
- Guhathakurta, P., Rich, R. M., Reitzel, D. B., Cooper, M. C., Gilbert, K., Majewski, S. R., Ostheimer, J. C., Geha, M. C., Johnston, K. V., & Patterson, R. J. 2005, *AJ*, in press (astro-ph/0406145)
- Ibata, R., Irwin, M. J., Ferguson, A. M. N., Lewis, G., & Tanvir, N. 2001a, *Nature*, 412, 49
- Ibata, R., Lewis, G. F., Irwin, M. J., Totten, E., & Quinn, T. 2001b, *ApJ*, 551, 294
- Ibata, R., Chapman, S., Ferguson, A. M. N., Irwin, M., Lewis, G., & McConnachie, A. 2004, *MNRAS*, 351, 117
- Johnston, K. V. 1998, *ApJ*, 495, 297
- Johnston, K. V., Sackett, P. D., & Bullock, J. S. 2001, *ApJ*, 557, 137
- Johnston, K. V., Law, D. R., & Majewski, S. R. 2005, *ApJ*, 619, 800
- Landau, L. D., & Lifschitz, E. M. 1976, "Mechanics", Pergamon, Oxford
- Law, D. R., Johnston, K. V., & Majewski, S. R. 2005, *ApJ*, 619, 807
- Mateo, M. L. 1998, *ARAA*, 36, 435
- Martínez-Delgado, D., Gómez-Flechoso, M. Á., Aparicio, A., & Carrera, R. 2004, *ApJ*, 601, 242
- McConnachie, A. W., Irwin, M. J., Ibata, R. A., Ferguson, A. M. N., Lewis, G. F., & Tanvir, N. 2003, *MNRAS*, 343, 1335
- McConnachie, A. W., Irwin, M. J., Lewis, G. F., Ibata, R. A., Chapman, S. C., Ferguson, A. M. N., & Tanvir, N. R. 2004, *MNRAS*, 351, L94
- Merrett, H. R., et al. 2003, *MNRAS*, 346, L62
- Merrett, H., et al. 2004, in Proc. of ESO-Workshop "Planetary Nebulae beyond the Milky Way", eds. J. R. Walsh and L. Stanghellini, Springer-Verlag (astro-ph/0407331)
- Morrison, H. L., Harding, P., Hurley-Keller, D., & Jacoby, G. 2003, *ApJ*, 596, L183
- Peebles, P. J. E., Phelps, S. D., Shaya, E. J., & Tully, R. B. 2001, *ApJ*, 554, 104
- De Rijcke, S., Michielsen, D., Dejonghe, H., Zeilinger, W. W., & Hau, G. K. T. 2005, *A&A*, 438, 491
- Stadel, J. 2001, Ph.D. Thesis, University of Washington, Seattle, WA, USA
- Stanek, K. Z., & Garnavich, P. M. 1998, *ApJ*, 503, 131L
- Taylor, J. E., & Babul, A. 2001, *ApJ*, 559, 716
- Totten, E. J. & Irwin, M. J. 1998, *MNRAS*, 294, 1
- de Vaucouleurs, G., de Vaucouleurs, A., Corwin, H., Buta, R., Paturel, G., & Fouque, P., 1991, "Third Reference Catalogue of Bright Galaxies", Springer-Verlag, Berlin/Heidelberg/New York
- Wadsley, J. W., Stadel, J., & Quinn, T. 2004, *New Astronomy*, 9, 137
- Zucker, D. B., et al. 2004, *ApJ*, 612, L117